Supplementary information

Experimental signature of the parity anomaly in a semi-magnetic topological insulator

Supplementary Information for

Experimental signature of parity anomaly in semi-magnetic topological insulator

M. Mogi, Y. Okamura, M. Kawamura, R. Yoshimi, K. Yasuda,

A. Tsukazaki, K. S. Takahashi, T. Morimoto, N. Nagaosa,

M. Kawasaki, Y. Takahashi, and Y. Tokura

Contents:

I. Correspondence between the parity anomaly and the semi-magnetic TI.

The parity anomaly is a concept first introduced to 2D Dirac fermions in quantum field theory[1-6]. First, we consider a single species of Dirac fermions in a 2D space. When the Dirac fermions are massless, they possess parity symmetry (Fig. S1A), whereas the parity symmetry, as well as the time-reversal symmetry, is broken when a Dirac fermion acquires a mass (Fig. S1B). Under an electromagnetic field perturbation (which corresponds to the THz light in this study), the massive Dirac fermions exhibit a parity-violating current, which results in the half-quantized Hall conductance. Peculiarly, while the massless Dirac fermion system preserves the parity symmetry, an infinitesimally small mass brings about the half-quantized Hall conductance where its sign depends on the sign of the infinitesimal mass. Thus, the half-quantized Hall conductance is recognized as a signature of the parity anomaly.

In 2D lattice models and real materials, however, the fermion doubling[7] requires that the Dirac fermions appear in pairs, which has made the observation of the parity anomaly or half quantized Hall conductance a challenging task. Namely, if a pair of Dirac fermions are both massive, the half-quantized Hall conductivities either add up to an integer (+1 or -1) or cancel out (0), and one cannot directly measure the half-quantized Hall conductance.

To observe the parity anomaly (or half-quantized Hall conductance) arising from a single Dirac fermion system in the low-energy region, it is necessary to induce a gap only in one of the paired Dirac fermions by breaking parity symmetry and time-reversal symmetry simultaneously. In a 3D TI, the massless and massive Dirac fermions can be realized at the bottom and top surfaces, respectively (Fig. 1a,b). This naturally requires a structure with broken inversion symmetry as a 3D system. Because the parity anomaly itself is purely a property of 2D Dirac fermions at the surface as described above, it is not affected by details of the bulk part, as far as the bulk state is a topological insulating state and supports the Dirac surface states. Rather, one needs to engineer a suitable inversion symmetry broken 3D structure to realize the single massless Dirac fermion and to observe the half-integer quantum Hall effect by tuning the semi-magnetic structure as well as the chemical potential within the mass gap.
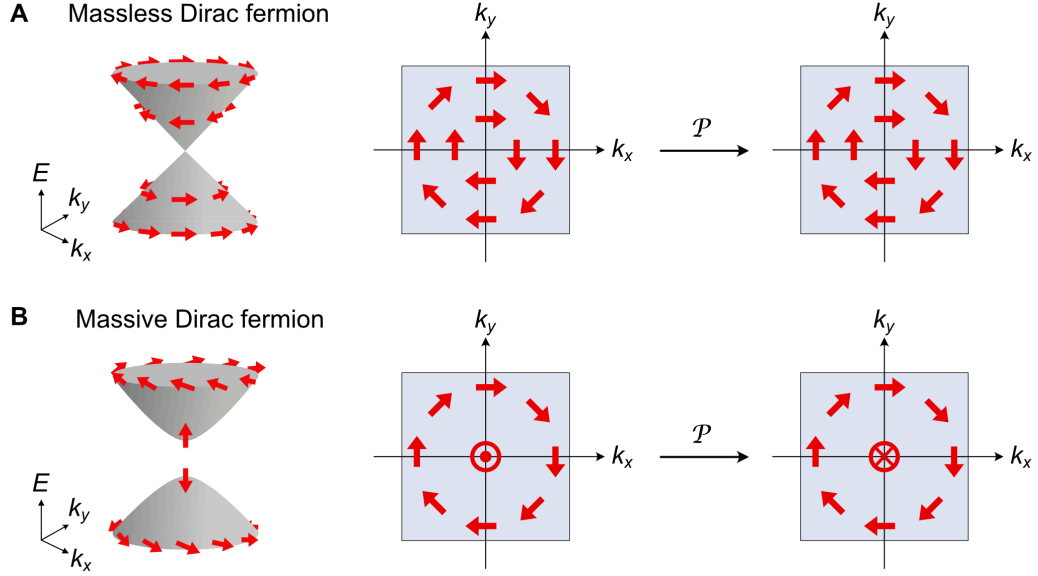
Fig. S1. Parity symmetry of 2D Dirac fermions. (**A**) Parity-symmetric massless Dirac fermion. The Hamiltonian of the massless Dirac fermion is defined as $H_0(k_x, k_y) = \hbar(\sigma_x k_y - \sigma_y k_x)$. When the 2D parity operation (or reflection of one spatial coordinate) transforms $k_x \rightarrow -k_x$, $\mathcal{P}H_0(-k_x, k_y)\mathcal{P}^{-1} = H(k_x, k_y)$ is satisfied. Here, $\mathcal{P} = i\sigma_x$ is the parity operator and $\mathcal{P}(\sigma_x, \sigma_y, \sigma_z)\mathcal{P}^{-1} = (\sigma_x, -\sigma_y, -\sigma_z)$. (**B**) Parity-symmetry-broken massive Dirac fermion. The Hamiltonian is defined as $H_m(k_x, k_y, m) = \hbar(\sigma_x k_y - \sigma_y k_x) + m\sigma_z$, where $\mathcal{P}H_m(-k_x, k_y, m)\mathcal{P}^{-1} = H_m(k_x, k_y, -m) \neq H_m(k_x, k_y, m)$, indicating the broken parity symmetry due to the mass term.

II. Design of the semi-magnetic TI heterostructures.

In the semi-magnetic structure of Fig. S2C (the same as Fig. 1b in the main text), we adopted the total thickness of 10 nm to suppress the hybridization between the top and bottom surface states[8] (we discuss the impact of the hybridization in section X). Firstly, we optimized the composition of Bi, Sb, and Cr by using the sandwich structure films hosting the QAH effect[9,10] (Fig. S2A) to keep E_F within the magnetic gap of the surface states (Fig. S2B). Those parameters were adjusted such that they exhibit the QAH effect at around 2 K (Fig. 3 in the main text). Then, the top two layers of the semi-magnetic structure of Fig. S2B [2-nm $Cr_{0.24}(Bi_{0.27}Sb_{0.73})_{1.76}Te_3$/3-nm-thick $(Bi_{0.27}Sb_{0.73})_2Te_3$)] is kept the same as that for the sandwich structure, while the Bi/Sb composition x of the bottom half region is varied to some extent ($x = 0.73$-0.93) without magnetic (Cr) doping, which still keeps the Fermi level within the bulk band gap (~200 meV). Here, the thickness of the 3-nm-thick $(Bi_{0.27}Sb_{0.73})_2Te_3$ is thick enough to suppress a possible carrier transfer from the bottom surface and the 5-nm-thick $(Bi_{1-x}Sb_x)_2Te_3$ layer especially when the bulk state is insulating (Fig. S2D). To ensure that E_F lies

within the magnetic gap, we conducted gate voltage (V_g) dependent transport experiments for several samples and confirmed that σ_{xy} already took the maximum region at around $V_g = 0$ V as shown in Fig. S6 (see section V for details). Note that the Cr concentration (12%) calibrated by beam equivalent pressures for the film growth (see Methods) might be close to the critical value of the non-trivial to trivial insulator transition[11] due to the weakened spin-orbit coupling by Cr atoms[12]. However, our undoped TI layer is thick (8 nm) enough to support the topologically non-trivial regime and does not affect our conclusion.
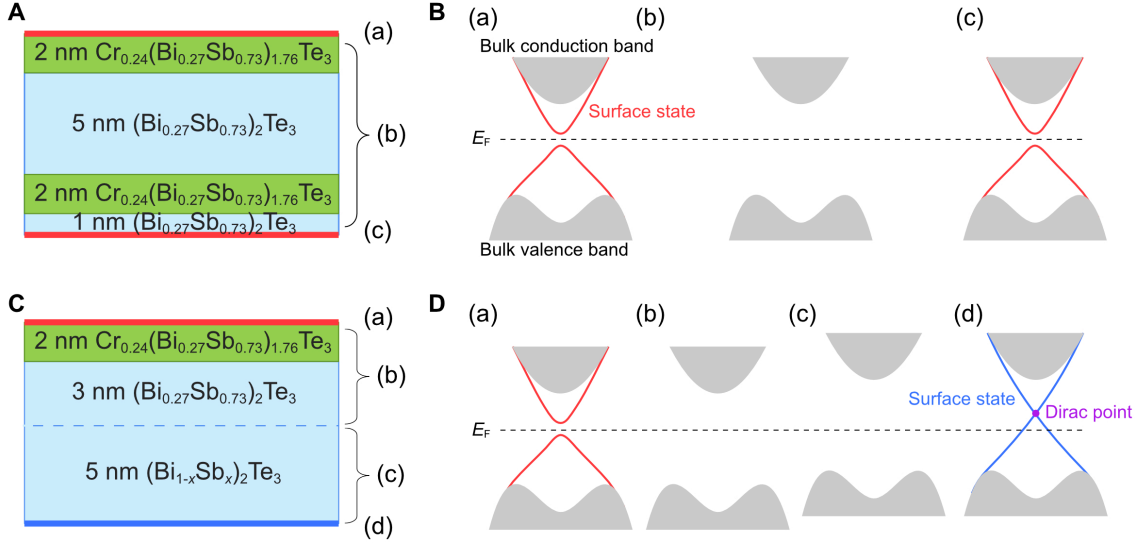
Fig. S2. Heterostructure engineering of magnetically doped TI films. (**A**) Schematic layout of a magnetic TI film that exhibits the quantized Faraday/Kerr rotations (Fig. 2c,d in the main text and Extended Data Fig. 1). (**B**) Band diagrams for the magnetic TI depicted in (A). (a-c) corresponds to the layer positions indicated in (A). (**C**) Schematic layout of a semi-magnetic topological insulator film, which is the same as Fig. 1b in the main text. (**D**) Band diagrams for the semi-magnetic TI depicted in (C) when $x > 0.73$. (a-d) corresponds to the layer positions indicated in (C).

III. Derivation of the Faraday and Kerr rotation angles.

We derive the low-energy limit of Faraday and Kerr rotation angles for a model of the semi-magnetic TI on a substrate as shown in Fig. S3. By using boundary conditions for the electric and magnetic fields traveling across the film and the substrate, we construct a transfer matrix of the light polarization[13].

We first consider that the light propagates along z-direction and is transmitted through the interfaces (x-y plane) with electrical conductivities σ_{xx} and σ_{xy}. We define the transfer matrix (T^I) connecting between the electric fields at the left-hand side (L) and those at the right-hand side (R) of the interface:

$$\begin{pmatrix} E_x^{+\mathrm{R}} \\ E_y^{+\mathrm{R}} \\ E_x^{-\mathrm{R}} \\ E_y^{-\mathrm{R}} \end{pmatrix} = \mathrm{T}^{\mathrm{I}} \begin{pmatrix} E_x^{+\mathrm{L}} \\ E_y^{+\mathrm{L}} \\ E_x^{-\mathrm{L}} \\ E_y^{-\mathrm{L}} \end{pmatrix}, \tag{S1}$$

where $+$ $(-)$ denotes the direction of the light propagation, $+z$ $(-z)$. T^{I} is derived by using the boundary conditions for the electric and magnetic fields following the Maxwell equations: $\nabla \times \boldsymbol{E} = -\partial \boldsymbol{B}/\partial t$, and $\nabla \times \boldsymbol{H} = \boldsymbol{j} + \partial \boldsymbol{D}/\partial t = \sigma \boldsymbol{E}\delta(z - z_0) + \varepsilon\, \partial \boldsymbol{E}/\partial t$, where ε is a dielectric constant of the medium, z_0 is the position of the interface, and σ is the 2×2 electrical conductivity tensor at the interface. Then, the boundary conditions are given by,

$$\boldsymbol{E}^{\mathrm{L}} - \boldsymbol{E}^{\mathrm{R}} = 0, \tag{S2}$$

$$\hat{z} \times (\boldsymbol{H}^{\mathrm{L}} - \boldsymbol{H}^{\mathrm{R}}) = \sigma \boldsymbol{E}^{\mathrm{L}} = \sigma \boldsymbol{E}^{\mathrm{R}}, \tag{S3}$$

where $\hat{z}$ is the unit vector along the $+z$, c is the speed of light, ω is the frequency of light, n is the refractive index of the medium, and $\boldsymbol{E}^{\mathrm{L(R)}}$ and $\boldsymbol{H}^{\mathrm{L(R)}}$ are the left (right) hand side of electric and magnetic fields, respectively. By approximating the relative permeability constant in each region to 1, the electric and magnetic fields are given by $\boldsymbol{E}^{\pm\mathrm{L(R)}} = \boldsymbol{E}_0^{\pm\mathrm{L(R)}} e^{i(\pm k_z z + \omega t)}$ and $\boldsymbol{B}^{\pm\mathrm{L(R)}} (= \mu_0 \boldsymbol{H}^{\pm\mathrm{L(R)}}) = \pm\frac{n}{c}\hat{z} \times \boldsymbol{E}^{\pm\mathrm{L(R)}}$, where $k_z = n\omega/c$ is the wavenumber of light.

By using Eqs. S1-S3, $\mathrm{T}^{\mathrm{I}}(n_{\mathrm{L}}, n_{\mathrm{R}}, \sigma_{xx}, \sigma_{xy})$ ($n_{\mathrm{L(R)}}$ is the refractive index of the left- (right-) hand side of the medium and σ_{xx}, σ_{xy} are conductivities in a unit of e^2/h) is described by

$$\mathrm{T}^{\mathrm{I}} = \frac{1}{2} \begin{pmatrix} 1 + \dfrac{n_{\mathrm{L}}}{n_{\mathrm{R}}} - \dfrac{2\alpha\sigma_{xx}}{n_{\mathrm{R}}} & -\dfrac{2\alpha\sigma_{xy}}{n_{\mathrm{R}}} & 1 - \dfrac{n_{\mathrm{L}}}{n_{\mathrm{R}}} - \dfrac{2\alpha\sigma_{xx}}{n_{\mathrm{R}}} & -\dfrac{2\alpha\sigma_{xy}}{n_{\mathrm{R}}} \\ \dfrac{2\alpha\sigma_{xy}}{n_{\mathrm{R}}} & 1 + \dfrac{n_{\mathrm{L}}}{n_{\mathrm{R}}} - \dfrac{2\alpha\sigma_{xx}}{n_{\mathrm{R}}} & \dfrac{2\alpha\sigma_{xy}}{n_{\mathrm{R}}} & 1 - \dfrac{n_{\mathrm{L}}}{n_{\mathrm{R}}} - \dfrac{2\alpha\sigma_{xx}}{n_{\mathrm{R}}} \\ 1 - \dfrac{n_{\mathrm{L}}}{n_{\mathrm{R}}} + \dfrac{2\alpha\sigma_{xx}}{n_{\mathrm{R}}} & \dfrac{2\alpha\sigma_{xy}}{n_{\mathrm{R}}} & 1 + \dfrac{n_{\mathrm{L}}}{n_{\mathrm{R}}} + \dfrac{2\alpha\sigma_{xx}}{n_{\mathrm{R}}} & \dfrac{2\alpha\sigma_{xy}}{n_{\mathrm{R}}} \\ -\dfrac{2\alpha\sigma_{xy}}{n_{\mathrm{R}}} & 1 - \dfrac{n_{\mathrm{L}}}{n_{\mathrm{R}}} + \dfrac{2\alpha\sigma_{xx}}{n_{\mathrm{R}}} & -\dfrac{2\alpha\sigma_{xy}}{n_{\mathrm{R}}} & 1 + \dfrac{n_{\mathrm{L}}}{n_{\mathrm{R}}} + \dfrac{2\alpha\sigma_{xx}}{n_{\mathrm{R}}} \end{pmatrix}, \tag{S4}$$

where α is the fine structure constant ($\alpha = e^2/2\epsilon_0 hc$). Then, considering the interference of the light due to multi-reflections inside the film, the transfer matrix T^{B} for the propagation in the TI bulk with thickness d is given by

$$\mathrm{T}^{\mathrm{B}} = \begin{pmatrix} e^{ik_z d} & 0 & 0 & 0 \\ 0 & e^{ik_z d} & 0 & 0 \\ 0 & 0 & e^{-ik_z d} & 0 \\ 0 & 0 & 0 & e^{-ik_z d} \end{pmatrix}, \tag{S5}$$

where k_z is the wavenumber of the light propagating to the TI film, d is the thickness of the film. Since we consider the long-wavelength (low-frequency) limit ($k_z d \to 0$), $\mathrm{T}^{\mathrm{B}} = \mathrm{I}$, where I is the identity matrix.

In the situation of the Faraday rotation measurement for a TI thin film on a substrate (Fig. S3A), the incident light is polarized along x. Then, the transmitted and reflected light are related by the following equation:

$$\begin{pmatrix} E_x^t \\ E_y^t \\ 0 \\ 0 \end{pmatrix} = \mathrm{T}^{\text{total}} \begin{pmatrix} E_x^i \\ 0 \\ E_x^r \\ E_y^r \end{pmatrix}. \tag{S6}$$

The total transfer matrix $\mathrm{T}^{\text{total}}$ is given by the product of Eqs. S4 and S5,

$$\mathrm{T}^{\text{total}} = \mathrm{T}^{\mathrm{I}}\left(n_{\mathrm{f}}, n_{\mathrm{s}}, \sigma_{xx}^{\mathrm{b}}, 0\right) \mathrm{T}^{\mathrm{B}} \mathrm{T}^{\mathrm{I}}\left(n_{\mathrm{v}}, n_{\mathrm{f}}, 0, \sigma_{xy}^{\mathrm{t}}\right)$$

$$= \frac{1}{2} \begin{pmatrix} 1 + \dfrac{n_{\mathrm{v}}}{n_{\mathrm{s}}} - \dfrac{2\alpha\sigma_{xx}^{b}}{n_{\mathrm{s}}} & -\dfrac{2\alpha\sigma_{xy}^{t}}{n_{\mathrm{s}}} & 1 - \dfrac{n_{\mathrm{v}}}{n_{\mathrm{s}}} - \dfrac{2\alpha\sigma_{xx}^{b}}{n_{\mathrm{s}}} & -\dfrac{2\alpha\sigma_{xy}^{t}}{n_{\mathrm{s}}} \\[2mm] \dfrac{2\alpha\sigma_{xy}^{t}}{n_{\mathrm{s}}} & 1 + \dfrac{n_{\mathrm{v}}}{n_{\mathrm{s}}} - \dfrac{2\alpha\sigma_{xx}^{b}}{n_{\mathrm{s}}} & \dfrac{2\alpha\sigma_{xy}^{t}}{n_{\mathrm{s}}} & 1 - \dfrac{n_{\mathrm{v}}}{n_{\mathrm{s}}} - \dfrac{2\alpha\sigma_{xx}^{b}}{n_{\mathrm{s}}} \\[2mm] 1 - \dfrac{n_{\mathrm{v}}}{n_{\mathrm{s}}} + \dfrac{2\alpha\sigma_{xx}^{b}}{n_{\mathrm{s}}} & \dfrac{2\alpha\sigma_{xy}^{t}}{n_{\mathrm{s}}} & 1 + \dfrac{n_{\mathrm{v}}}{n_{\mathrm{s}}} + \dfrac{2\alpha\sigma_{xx}^{b}}{n_{\mathrm{s}}} & \dfrac{2\alpha\sigma_{xy}^{t}}{n_{\mathrm{s}}} \\[2mm] -\dfrac{2\alpha\sigma_{xy}^{t}}{n_{\mathrm{s}}} & 1 - \dfrac{n_{\mathrm{v}}}{n_{\mathrm{s}}} + \dfrac{2\alpha\sigma_{xx}^{b}}{n_{\mathrm{s}}} & -\dfrac{2\alpha\sigma_{xy}^{t}}{n_{\mathrm{s}}} & 1 + \dfrac{n_{\mathrm{v}}}{n_{\mathrm{s}}} + \dfrac{2\alpha\sigma_{xx}^{b}}{n_{\mathrm{s}}} \end{pmatrix}. \tag{S7}$$

By substituting Eq. S7 to Eq. S6,

$$\begin{cases} 2E_x^t = \left(1 + \dfrac{n_{\mathrm{v}}}{n_{\mathrm{s}}} - \dfrac{2\alpha\sigma_{xx}^{b}}{n_{\mathrm{s}}}\right) E_x^i + \left(1 - \dfrac{n_{\mathrm{v}}}{n_{\mathrm{s}}} - \dfrac{2\alpha\sigma_{xx}^{b}}{n_{\mathrm{s}}}\right) E_x^r - \dfrac{2\alpha\sigma_{xy}^{t}}{n_{\mathrm{s}}} E_y^r, \\[3mm] 2E_y^t = \dfrac{2\alpha\sigma_{xy}^{t}}{n_{\mathrm{s}}} E_x^i + \dfrac{2\alpha\sigma_{xy}^{t}}{n_{\mathrm{s}}} E_x^r + \left(1 - \dfrac{n_{\mathrm{v}}}{n_{\mathrm{s}}} - \dfrac{2\alpha\sigma_{xx}^{b}}{n_{\mathrm{s}}}\right) E_y^r, \\[3mm] 0 = \left(1 - \dfrac{n_{\mathrm{v}}}{n_{\mathrm{s}}} + \dfrac{2\alpha\sigma_{xx}^{b}}{n_{\mathrm{s}}}\right) E_x^i + \left(1 + \dfrac{n_{\mathrm{v}}}{n_{\mathrm{s}}} + \dfrac{2\alpha\sigma_{xx}^{b}}{n_{\mathrm{s}}}\right) E_x^r + \dfrac{2\alpha\sigma_{xy}^{t}}{n_{\mathrm{s}}} E_y^r, \\[3mm] 0 = -\dfrac{2\alpha\sigma_{xy}^{t}}{n_{\mathrm{s}}} E_x^i - \dfrac{2\alpha\sigma_{xy}^{t}}{n_{\mathrm{s}}} E_x^r + \left(1 + \dfrac{n_{\mathrm{v}}}{n_{\mathrm{s}}} + \dfrac{2\alpha\sigma_{xx}^{b}}{n_{\mathrm{s}}}\right) E_y^r. \end{cases} \tag{S8}$$

Finally, we get the Faraday rotation angle as,

$$\tan\theta_{\mathrm{F}} = \frac{E_y^{\mathrm{t}}}{E_x^{\mathrm{t}}} = \frac{2\alpha\sigma_{xy}^{t}}{n_s + n_v + 2\alpha\sigma_{xx}^{b}}. \tag{S9}$$

On the other hand, for the Kerr rotation measurement (Fig. S3B), the incident light comes from the substrate side. In this case, the total transfer matrix is rewritten as

$$\mathrm{T^{total}} = \mathrm{T^I}\left(n_f, n_v, 0, \sigma_{xy}^t\right)\mathrm{T^B}\mathrm{T^I}\left(n_s, n_f, \sigma_{xx}^b, 0\right)$$

$$= \frac{1}{2}\begin{pmatrix} 1 + \dfrac{n_s}{n_v} - \dfrac{2\alpha\sigma_{xx}^b}{n_v} & -\dfrac{2\alpha\sigma_{xy}^t}{n_v} & 1 - \dfrac{n_s}{n_v} - \dfrac{2\alpha\sigma_{xx}^b}{n_v} & -\dfrac{2\alpha\sigma_{xy}^t}{n_v} \\[2ex] \dfrac{2\alpha\sigma_{xy}^t}{n_v} & 1 + \dfrac{n_s}{n_v} - \dfrac{2\alpha\sigma_{xx}^b}{n_v} & \dfrac{2\alpha\sigma_{xy}^t}{n_v} & 1 - \dfrac{n_s}{n_v} - \dfrac{2\alpha\sigma_{xx}^b}{n_v} \\[2ex] 1 - \dfrac{n_s}{n_v} + \dfrac{2\alpha\sigma_{xx}^b}{n_v} & \dfrac{2\alpha\sigma_{xy}^t}{n_s} & 1 + \dfrac{n_s}{n_v} + \dfrac{2\alpha\sigma_{xx}^b}{n_v} & \dfrac{2\alpha\sigma_{xy}^t}{n_v} \\[2ex] -\dfrac{2\alpha\sigma_{xy}^t}{n_v} & 1 - \dfrac{n_s}{n_v} + \dfrac{2\alpha\sigma_{xx}^b}{n_v} & -\dfrac{2\alpha\sigma_{xy}^t}{n_v} & 1 + \dfrac{n_s}{n_v} + \dfrac{2\alpha\sigma_{xx}^b}{n_v} \end{pmatrix}, (S10)$$

in which n_s is just interchanged with n_v for Eq. S7. Thus, the Kerr rotation angle is described by

$$\tan\theta_{\mathrm{K}} = \frac{E_y^r}{E_x^r} = \frac{4\alpha n_s \sigma_{xy}^t}{n_s{}^2 - n_v{}^2 + 4\alpha n_v \sigma_{xx}^b + 4\alpha^2\left(\sigma_{xx}^b{}^2 + \sigma_{xy}^t{}^2\right)}. \tag{S11}$$

To better clarify the contribution of the bottom surface transport (σ_{xx}^b), we plot θ_{F} and θ_{K} versus σ_{xx}^b in Fig. S4 by substituting $n_v = 1$ and $n_s = 3.46$ (for InP substrates) and $\sigma_{xy}^t = 1/2\ (e^2/h)$ to Eqs. S9 and S10. Even in the presence of finite $\sigma_{xx}{}^b$, θ_{F} and θ_{K} take almost constant values. For the typical semi-magnetic TI films with $\sigma_{xx}^b \sim 1(e^2/h)$, the error from the half-quantized value with $\sigma_{xx}^b \sim 0$ amounts to only 0.3% (0.3%) for the Faraday (Kerr) rotation. Even for the case of $\sigma_{xx}^b \sim 4(e^2/h)$, which is the largest value presented in the main text (Fig. 3), the error is only 1.3% (1.1%). Thus, the Faraday (Kerr) rotation is insensitive to σ_{xx}^b in the semi-magnetic TI. Therefore, the Faraday (Eq. S9) and Kerr rotation (Eq. S11) angles can be reasonably approximated to,

$$\theta_{\mathrm{F}} \approx \arctan\left(\frac{\alpha}{n_s + 1}\right), \tag{S12}$$

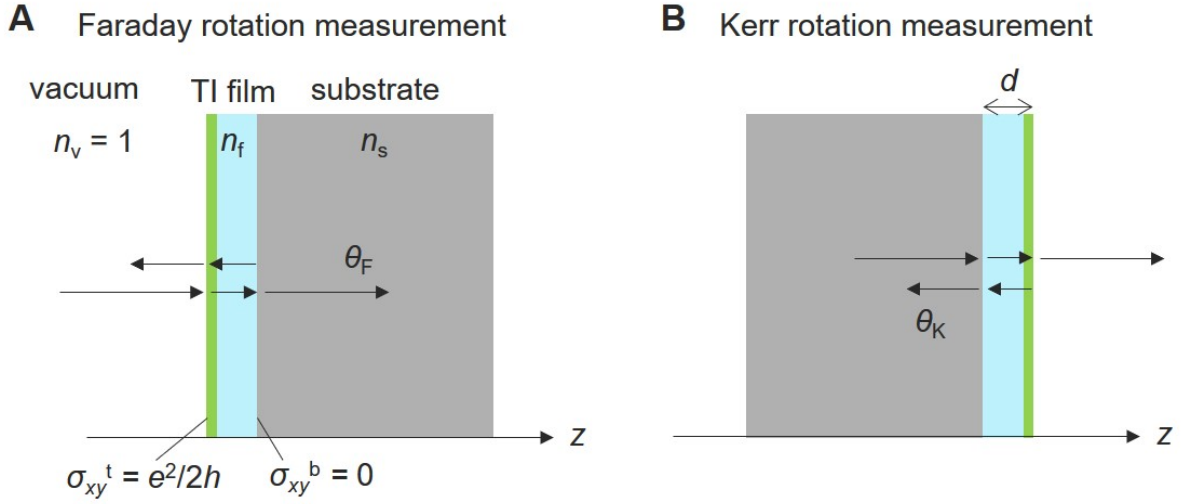$$\theta_{\mathrm{K}} \approx \arctan\left(\frac{2\alpha n_s}{n_s{}^2 - 1}\right). \tag{S13}$$

Compared with the quantized Faraday and Kerr rotation angles in the Q(A)H states as calculated previously[13-18],

$$\theta_{\mathrm{F}}^{\mathrm{Q}} = \arctan\left(\frac{2\alpha}{n_s + 1}\right), \tag{S14}$$

$$\theta_{\mathrm{K}}^{\mathrm{Q}} = \arctan\left(\frac{4\alpha n_s}{n_s{}^2 - 1 + 4\alpha^2}\right) \approx \arctan\left(\frac{4\alpha n_s}{n_s{}^2 - 1}\right), \tag{S15}$$

the calculated rotation angles for the semi-magnetic TI films give rise to half of the integer-quantized rotations $\theta_{\mathrm{F}}^{\mathrm{Q}}$ and $\theta_{\mathrm{K}}^{\mathrm{Q}}$, corresponding to our experimental results.

A Faraday rotation measurement

vacuum   TI film   substrate

$n_v = 1$ n_f n_s

θ_F

z

$\sigma_{xy}{}^t = e^2/2h$ $\sigma_{xy}{}^b = 0$

B Kerr rotation measurement

d

θ_K

z

Fig. S3. Semi-magnetic TI model for the derivation of Faraday and Kerr rotations. (A) Schematic geometry for the Faraday rotation measurement in a TI/substrate structure. The light propagates along the z-axis from the vacuum of which a refractive index $n_v = 1$. The reflection occurs at the interfaces between the TI film and the vacuum ($\sigma_{xy}{}^t = 1/2\ (e^2/h)$ and $\sigma_{xx}{}^t = 0$) and between the TI film and the substrate ($\sigma_{xy}{}^b = 0$ and $\sigma_{xx}{}^b \neq 0$). The transmitted light experiences the Faraday rotation. **(B)** Schematic geometry for the Kerr rotation measurement where the light comes from the substrate side. The light reflects at the top and bottom surfaces of the film, experiencing the Kerr rotation without a time delay between them because the film thickness d which we consider is much shorter than the wavelength of light.
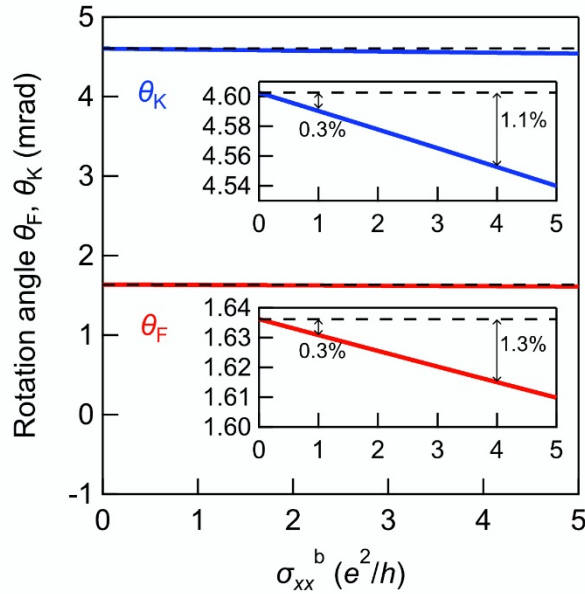
Fig. S4. Calculated Faraday and Kerr rotation angles in a semi-magnetic TI model.

Dependence of θ_F and θ_K on $\sigma_{xx}{}^b$, calculated by using Eqs. S9 and S11. The broken lines indicate the θ_F and θ_K for $\sigma_{xx}{}^b = 0$. The insets are magnified views for θ_F and θ_K.

IV. Discussion on the relationship between THz photon energy and the magnetic gap.

The magnetization gap as large as 10-30 meV (refs. 14,15) is known to have significant spatial fluctuations due to disorders such as electronic and magnetic inhomogeneities as studied with scanning tunneling microscopy[14,15], scanning SQUID[16], and magnetic force microscopy[17,18]. Such inhomogeneities are believed to be the major reason for the limitation of the low observable temperature of the QAH effect (< 2 K)[9]. Indeed, in transport experiments, the effective gap size as estimated by the thermal activation energy decreases to < 1 meV (refs. 8,10,19). However, if the reduced magnetic gap were reflected in the THz magneto-optical rotation angles, the quantization could not occur in our spectral region as follows[20,21]. Since there is a simple relation, $\theta_F + i\eta_F \sim \sigma_{xy}/\{(n_s + 1)c\varepsilon_0\}$ in the small rotation angle limit, it is important to consider the complex optical Hall conductivity. Assuming a 2D Dirac electronic state with the mass gap of m, the optical Hall conductivity $\sigma_{xy}(\omega)$ is described by[20,21]

$$\sigma_{xy}(\omega) = \frac{e^2}{2h}\frac{m}{\hbar\omega + i\gamma}\ln\left|\frac{-\hbar\omega - i\gamma + 2\max(|\mu|, m)}{\hbar\omega + i\gamma + 2\max(|\mu|, m)}\right|, \qquad (S16)$$

where γ and μ denote the damping constant and the chemical potential, respectively. We calculated $\sigma_{xy}(\omega)$ with various γ under the assumption of $2m = 30$ meV and $\mu = 0$ meV. As shown in Fig. S5A, if the THz photon energy is well below the induced gap, the real part of the optical Hall conductivity is quantized. On the other hand, if the THz photon energy is above the gap, the optical Hall conductivity, or the polarization rotation, gets smaller, irrespective of γ. In addition, there is a finite imaginary part (Fig. S5B), which results in the ellipticity. At the resonant frequency, both the real and imaginary parts of the optical Hall conductivity are enhanced while γ suppresses the enhancement. Thus, if the photon energy exceeds the magnetic gap size, the quantization and the nearly zero ellipticity are no longer obtained.

The key to resolving the discrepancy is the difference between transport and optical spectroscopy, where light is characterized by an electric field vector (light polarization) and photon energy. The polarization rotation angle reflects the optical Hall conductivity while the spectrum reflects interband transitions. Therefore, there is no contradiction in that the rotation angle is not quantized at high temperature as expected by the local magnetization gap estimations[14,15] whereas the spectrum is flat (or of no resonance feature) within a few THz range. Nevertheless, the direct optical detection of the magnetic gap with far- to mid-infrared light remains for future works[22].
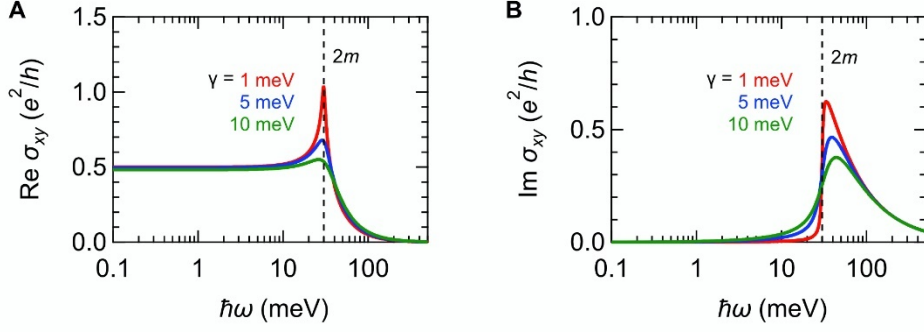
Fig. S5. Calculated optical Hall conductivity. (A,B) Real (A) and imaginary (B) part of the optical Hall conductivity calculated for a single 2D Dirac electronic state with mass gap $2m = 30$ meV and chemical potential $\mu = 0$ meV.

V. Gate voltage dependence on transport.

To confirm that E_F is kept within the magnetic gap, we have checked the top gate voltage (V_g) dependence on the electrical transport of the semi-magnetic TI films. In Figs. S6A-C, we show σ_{xy} and σ_{xx} versus V_g under various H for three samples ($x = 0.93$, 0.89 and 0.85), where x is the Sb fraction for the bottom 5-nm-thick $(Bi_{1-x}Sb_x)_2Te_3$ layer. At zero magnetic field, because the bottom surface is gapless, σ_{xy} (black lines) reflects the anomalous Hall effect of the top surface. In all the samples, the values of σ_{xy} at zero magnetic field are close to $0.5e^2/h$ for a wide range of V_g. These considerably large values cannot be achieved unless the E_F resides within the magnetization gap in these samples. If the E_F is outside the magnetization gap, the value of σ_{xy} would be much smaller and would strongly depend on the V_g as calculated in Fig. S11B. In particular, in the $x = 0.89$ (Fig. S6B) sample, σ_{xy} takes the maximum value at around $V_g = 0$ V. In addition, for the $x = 0.89$ sample, when the magnetic field is applied and the cyclotron gap is formed on the bottom surface, σ_{xy} approaches e^2/h smoothly at $V_g = 0$ V. This result indicates that the E_F resides in the magnetization gap of the top surface and also in the cyclotron gap of the bottom surface at 9 T. This magnetic field dependence also supports that E_F is kept within the magnetic gap on the top surface.

We next assign the band alignments of top and bottom surface states in the films. By the application of H, we can judge the carrier types at each V_g from the sign of the ordinary Hall effect. We can also roughly judge the position of the Landau levels thanks to the observation of the QH effect[23], where the zeroth Landau levels are formed at the bottom of the conduction band for the gapped Dirac cone and the Dirac point for the gapless Dirac cone. In the samples of $x = 0.93$ (Fig. S6A) and 0.89 (Fig. S6B), the $\nu = 1$ QH plateau appears, indicating that E_F is slightly lower than both the zeroth Landau levels at the V_g region. Also, we observed a charge-neutrality point at around $V_g = 5$ V for the sample of $x = 0.89$ and hence E_F is the closest to the Dirac point of the bottom surface state. Thus, we have assigned the band alignments of $x = 0.93$ and 0.89 as shown in the insets of Figs. S6A and S6B. In the sample of $x = 0.85$ (Fig. S6C),

which possesses n-type carriers, σ_{xy} approaches zero ($\nu = 0$ QH state) with increasing H, indicating that E_F is slightly lower the Dirac point of the bottom surface state than that of the magnetic gap of the top surface state.
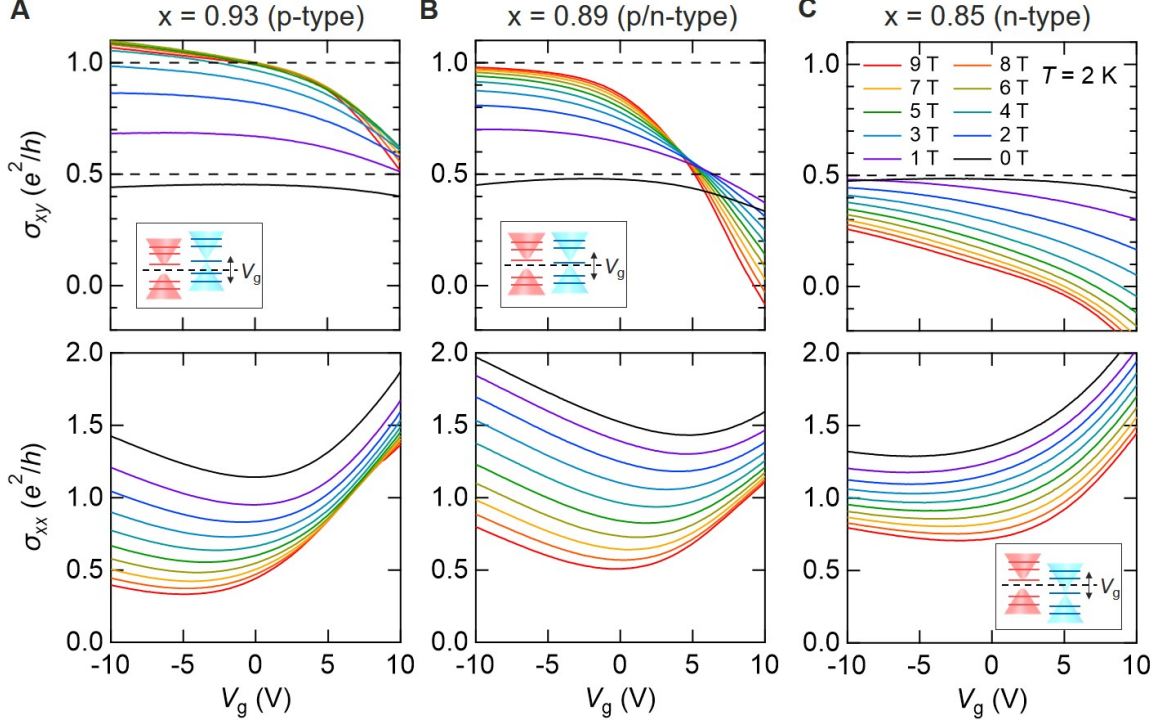

Fig. S6. Gate-voltage-dependent transport and determination of the band alignments in semi-magnetic TI films. (A-C) Top gate voltage (V_g) dependence of σ_{xy} and σ_{xx} at various magnetic fields and $T = 2$ K in semi-magnetic TI films of $x = 0.93$ (A), 0.89 (B) and 0.85 (C). The insets show schematics of the band alignments for the top (red) and bottom (blue) surface states (see the text in section V for the assignment).

VI. Additional magneto-transport data.

We have also performed the transport measurements under magnetic fields applied perpendicular to the films. Figure S7A shows the H dependence of ρ_{yx} at $T = 0.5$ K. In the samples of $x = 0.93$ and 0.89, $\nu = 1$ quantized Hall resistance was observed with the application of H (ref. 23). By converting from ρ_{yx} to σ_{xy} (Fig. S7C) using ρ_{xx} (Fig. S7B), σ_{xy} for the samples of $x = 0.85$ and 0.80 exhibit the insulating $\nu = 0$ QH states accompanied by the decrease of σ_{xx} (Fig. S7D). The observation of the QH effect indicates that E_F locates within the magnetic gap for the top surface, and at the same time, it locates near the Dirac points for the non-magnetic bottom surface. Figures S7E and S7F show the magnified views of the hysteresis behaviors at around $\mu_0 H = 0$ T. The sharp ferromagnetic reversals and the robust spontaneous anomalous Hall conductance support the single domain state at $\mu_0 H = 0$ T as presented in Figs. 2 and 3 in

the main text.
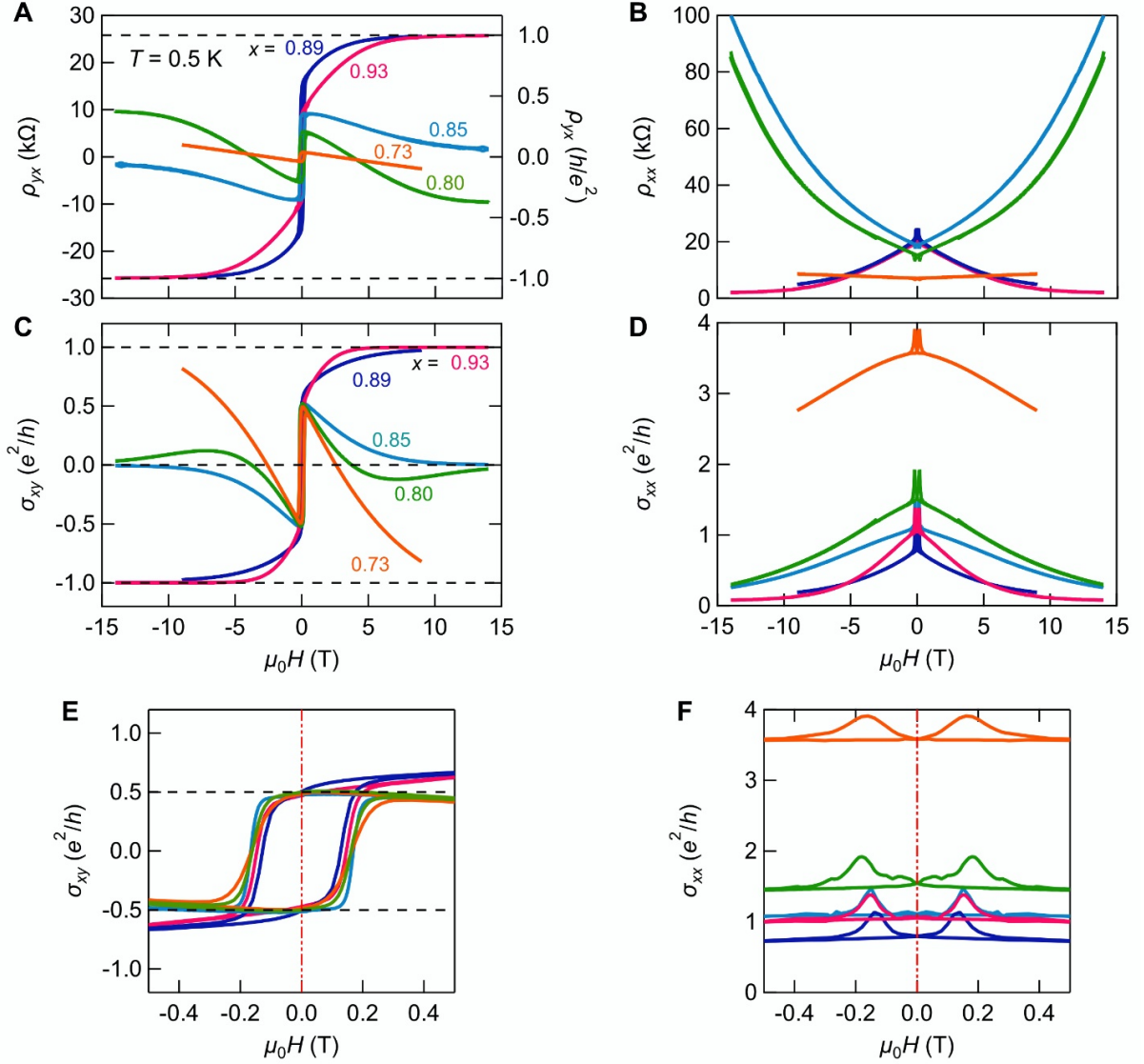
Fig. S7. Magneto-transport data in semi-magnetic TI films. (**A-D**) Magnetic field ($\mu_0 H$) dependence of ρ_{xx}, ρ_{yx} at 0.5 K in the semi-magnetic TI films with the variation of x, which are the identical films presented in Fig. 3 of the main text. (**E, F**) Magnified views of (C) and (D), respectively. The red dashed lines highlight the $\mu_0 H = 0$ T, where the half-integer quantization appears.

VII. Real-space picture of the Hall current and current distribution test in a multi-terminal device.

From the Berry curvature calculation in the momentum space picture, the gapped Dirac fermion in the top surface contributes to $\sigma_{xy} = e^2/(2h)$, and the gapless Dirac fermion in the bottom surface to $\sigma_{xy} = 0$, which is described in section X. In the real space picture, the Hall current is not carried by a single state like a chiral edge state as in the case of QHE, since there exist

12

gapless states in the bottom surface. Instead, the Hall current is carried by the gapless states that extend in the side surface and the bottom surface. This situation is analogous to the plateau to plateau transition in the ordinary QH system[24]. At the plateau transition in the QH system, there appear delocalized gapless states in the bulk and those states carry non-integer Hall current through the bulk. In the present case, the gapless Dirac fermion in the bottom surface plays the role of such delocalized gapless states that appear in the plateau transition of QHE. The key difference here is that the plateau transition in the ordinary QH system requires fine-tuning of the electron density or magnetic field to achieve $\sigma_{xy} = e^2/(2h)$ (see also Fig. S10 and section IX for discussions), while the parity anomaly in TIs does not require such fine-tuning of parameters.

To experimentally figure out the current distribution of the half-integer quantized transport, we conducted a three-terminal current flow measurement[25] using a multi-terminal device as shown in Fig. S8A. The device was made from a semi-magnetic TI film of $x = 0.93$ exhibiting $\nu = 1$ QH effect under the application of high magnetic fields H (Fig. S8B). In the measurement, we put a current of 100 nA from one of the electrodes and measure the current at the left-hand side (I_l), right-hand side (I_r), and opposite side (I_o) electrodes. Figure S8C shows the H dependence of the current flow at $T = 0.5$ K. In the QH state ($\mu_0 H \sim 14$ T), I_l (I_r) is much larger than I_r (I_l) at the positive (negative) H. This is due to the formation of chiral edge states which flow along with the counter-clockwise (clockwise) direction at the positive (negative) H. I_o is symmetric against the sign change of H because it originates from the remained surface conduction (σ_{xx}). By contrast, in the half-integer quantized state ($\mu_0 H = 0$ T), the difference between I_l and I_r dramatically diminishes. Upon closer look at the difference (see the inset of Fig. S8C), there are tiny hysteresis loops for I_l and I_r reflecting the anomalous Hall current. Moreover, we find that the centers of the hysteresis loops for I_l and I_r shift higher and lower, respectively. This shift can be attributed to the difference in the distance between the electrodes (200 μm and 400 μm from the center electrode to the left-hand side and right-hand side electrodes, respectively). Therefore, fully edge-localized chiral edge states are not formed in the half-integer quantized state.
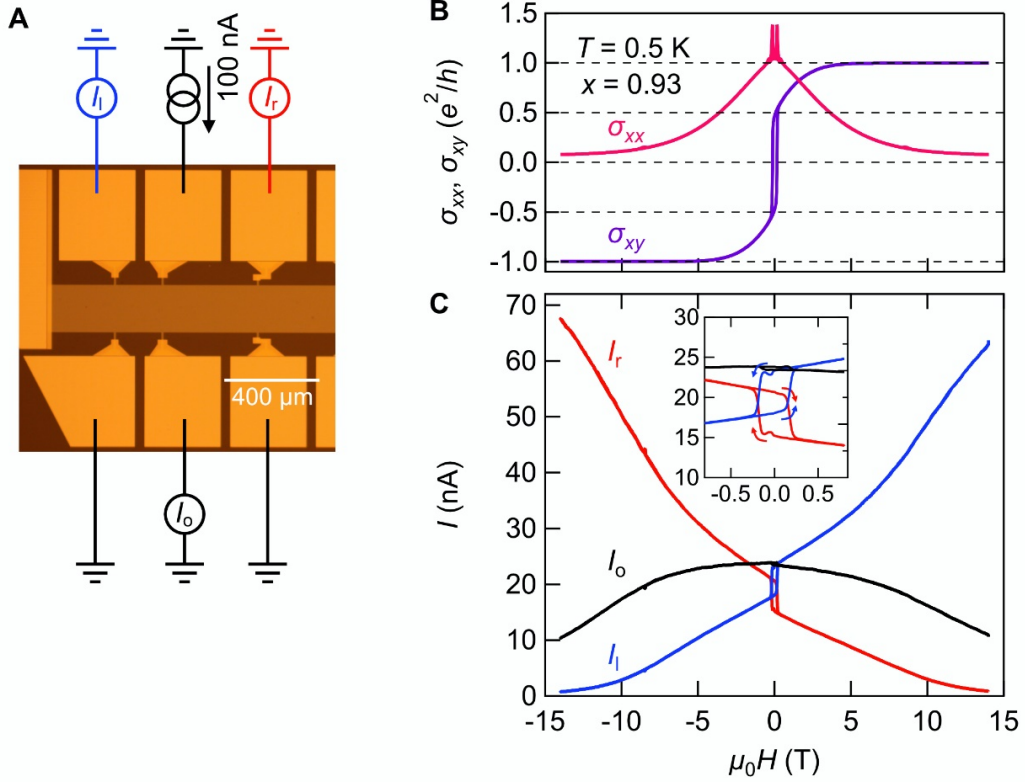
Fig. S8. Current distribution test in a multi-terminal device. (**A**) Optical microscope image of a multi-terminal Hall bar device. The excitation current is 100 nA in this measurement. (**B**) $\mu_0 H$ dependence of σ_{xx} and σ_{xy} at 0.5 K in the semi-magnetic TI film ($x = 0.93$). (**C**) $\mu_0 H$ dependence of the currents I_r, I_o, and I_l as indicated in a. The inset shows the magnified view of (C).

VIII. Scaling analysis of transport.

To understand the temperature dependence of the half-integer quantized transport in the semi-magnetic TI films, we map ($\sigma_{xy}(T)$, $\sigma_{xx}(T)$) and compare them with the theoretical curves for localization in usual 2D systems[26,27] and in 2D Dirac fermion systems[28] with broken time-reversal symmetries as shown in Figs. S9A and S9B, respectively. Whereas ($\sigma_{xy}(T)$, $\sigma_{xx}(T)$) for the QAH film follows a theoretical curve for the usual 2D system (Fig. S9A) as reported earlier[29], those for the semi-magnetic TI films converge to $\sigma_{xy} = 0.5e^2/h$. With even further decreasing the temperature, σ_{xy} show signatures to increase from $0.5e^2/h$. These behaviors contradict the scaling trajectory of the usual 2D system[26,27]. Instead, this can be viewed as the sum of the scaling behaviors for the two 2D Dirac fermions with magnetic impurities, where σ_{xx} approaches zero and half-quantized σ_{xy} becomes a stable fixed point for each of the Dirac fermion[28] (Fig. S9B). Since the effect of the magnetic impurities on the bottom surface is weak, the increase of its contribution to σ_{xy} is small even at the lowest temperature (blue arrow line in Fig. S9B); this is the reason why the plateau of σ_{xy} is observed. Furthermore, if the effect of

magnetic impurities on the bottom surface state is completely absent, σ_{xx} is expected to increase as the temperature is lowered[30]. Nonetheless, σ_{xx} decreases, and as the temperature is even lowered σ_{xy} tends to further increase slightly across this half-quantized value. Thus, these features indicate that the system is the almost decoupled two Dirac fermions with large (top surface) and small (bottom surface) σ_{xy} with broken time-reversal symmetry by finite size scaling at finite temperature.
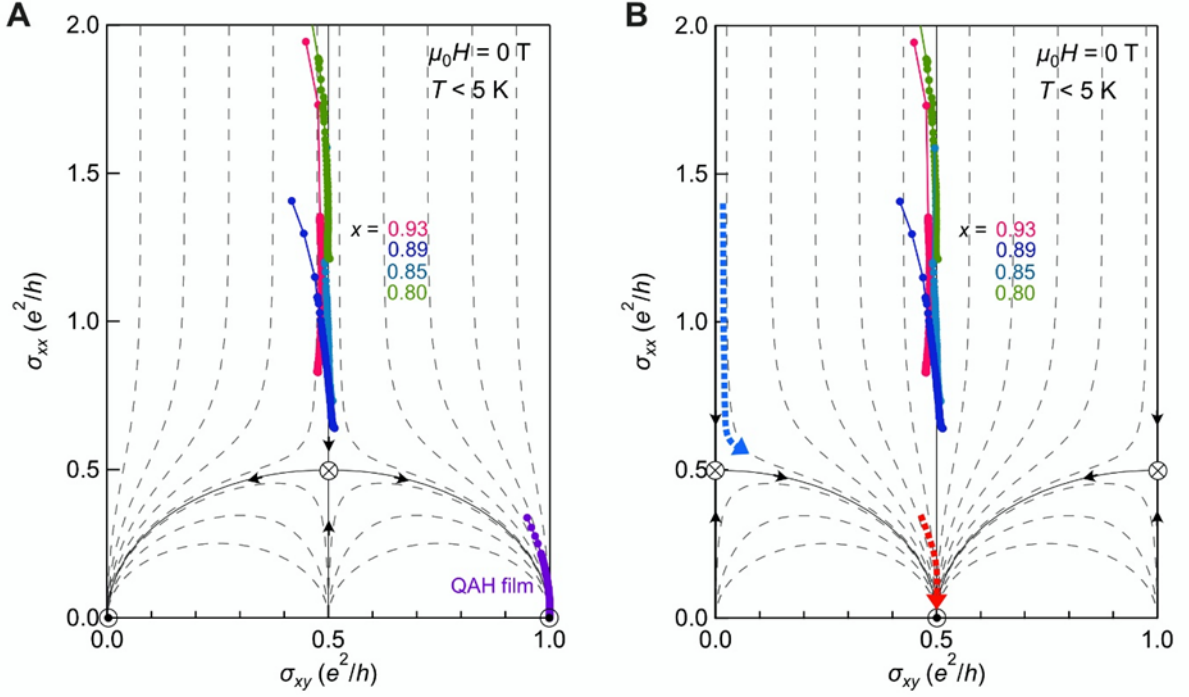

Fig. S9. Temperature-driven renormalization group flow. (A) Temperature-driven flows of $(\sigma_{xy}(T), \sigma_{xx}(T))$ for the semi-magnetic TI films ($x = 0.80, 0.85, 0.89$, and 0.93) and the QAH film. Broken lines show the renormalization group flow for conventional 2D systems, reproduced from ref. 27. **(B)** The same plots for the semi-magnetic TI films. The broken lines are the renormalization group flow for 2D Dirac fermion systems with broken time-reversal symmetry[28]. Red and blue broken arrow lines are the illustrations of flows describing the behaviors for the top and bottom surface Dirac fermions in the semi-magnetic TI, respectively.

IX. Difference between half-integer and integer quantized Hall states.

If the Fermi level was located exactly at a Landau level or there was a gapless state arising from disorders between the Landau levels in a conventional QH system, the Hall conductance would take arbitrary values. To observe the half-integer quantized Hall plateaus at zero magnetic field, however, a special mechanism must be required. In the semi-magnetic TI case, the parity anomaly from the top gapped surface state spontaneously tunes σ_{xy} at $e^2/(2h)$.

To experimentally clarify the difference between the half-integer and integer QH states, we investigated the V_g dependent transport properties at 0 T (half-quantized regime) and at 9 T (QH regime) of the semi-magnetic TI film ($x = 0.89$) at various cryogenic temperatures (0.04 – 0.7 K). We obtained σ_{xy} and σ_{xx} (Figs. S10C and S10D) from ρ_{yx} and ρ_{xx} (Figs. S10A and S10B). At zero magnetic field (Fig. S10C), the half-quantized σ_{xy} plateau is observed in a wide V_g range. On the other hand, at 9 T, it is observed only at a certain V_g (~ 7 V) while the $\nu = 1$ QH plateau appears in a wide V_g range. Furthermore, we map ($\sigma_{xy}(T)$, $\sigma_{xx}(T)$) at various V_g as shown in Figs. S10E and S10F in the same way as in Figs. S9A and S9B, respectively. On the mapping at 9 T (Fig. S10F), the trajectory follows the renormalization group flow of conventional 2D systems, where (σ_{xy}, σ_{xx}) flows to (0, 0) or (e^2/h, 0) by tuning the chemical potential across the Landau levels while $\sigma_{xy} = 0.5e^2/h$ corresponds to the critical line for the plateau-plateau transition of the conventional QH system (see the inset of Fig. S10D for the relationship between the magnetic gap and the Landau level position estimated by the field response, which is discussed in section IV). On the other hand, at 0 T (Fig. S10E), σ_{xy} converges and flows along $0.5e^2/h$ as discussed in section VIII even in the change of the chemical potential within the magnetic gap of the top surface. We note that the increase of ρ_{xx} with decreasing temperature at zero magnetic field (Fig. S10A) is consistent with the picture that our system is analogous to the plateau transition in the ordinary QH systems as discussed in section VII since ρ_{xx} also takes the maximum at the plateau transition in the QH effect. These zero-field half-quantized responses cannot be realized without the parity anomaly in TIs.
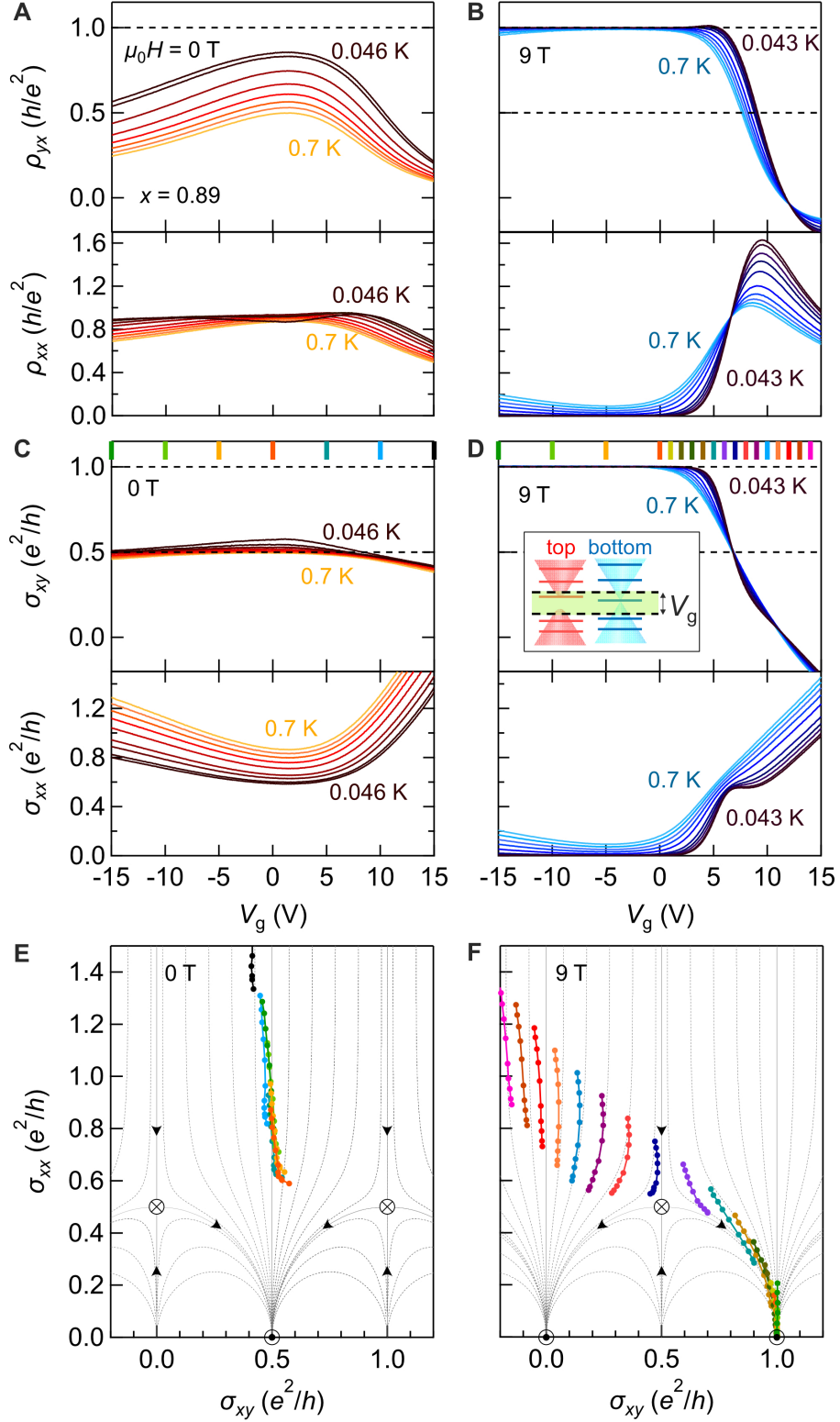
Fig. S10. (**A-D**) Gate voltage (V_g) dependence of ρ_{yx} and ρ_{yx} at $\mu_0 H = 0$ T (A) and 9 T (B), and of σ_{xy} and σ_{xx} at 0 T (C) and 9 T (D) for the semi-magnetic TI film ($x = 0.89$), measured at $T = 0.04 - 0.7$ K. The inset of (D) the schematic of the tunable V_g region (green shaded) for the band alignment of the semi-magnetic TI film ($x = 0.89$), which corresponds to Fig. S6B. (**E, F**) Temperature driven flows of ($\sigma_{xy}(T)$, $\sigma_{xx}(T)$) at 0 T (E) and 9 T (F). The colors of the plots for

(E) and (F) indicate the V_g values shown on the upper abscissa of (C) and (D) with the same color codes. The slight deviation from $\sigma_{xy} = e^2/(2h)$ toward e^2/h in (E) is attributed to be a tiny magnetic gap opening in the bottom surface state (see section VIII for the discussion).

X. Impact of the surface hybridization of the half-integer quantization.

We numerically and experimentally show that the half quantized Hall conductance is not maintained in the presence of the electronic hybridization between the top and bottom surface states.

Calculation

We here use an effective continuum model for the TI surface states (in *x-y* plane) including the top and bottom surface degrees of freedom[31]. The Hamiltonian for the wavevector $\boldsymbol{k} = (k_x, k_y)$, which is expressed in the $|t\uparrow\rangle, |t\downarrow\rangle, |b\uparrow\rangle$ and $|b\downarrow\rangle$ bases (*t* and *b* denote the top and bottom surface states, $\uparrow$ and $\downarrow$ represent the spin up and down states, respectively), can be written as

$$H(k_x, k_y) = \begin{pmatrix} \Delta_t & k_y - ik_x & m & 0 \\ k_y + ik_x & -\Delta_t & 0 & m \\ m & 0 & \Delta_b & -k_y + ik_x \\ 0 & m & -k_y - ik_x & -\Delta_b \end{pmatrix}, \quad \text{(S16)}$$

where m is a parameter for the hybridization gap, and Δ_t and Δ_b are magnetically-induced gaps for the top and bottom surfaces, respectively. Here, we set $\Delta_b = 0$ to express the situation of the semi-magnetic TI structure. By solving the eigen-equation for this Hamiltonian, the eigen-energies can be analytically obtained,

$$E = \pm \sqrt{\frac{\Delta_t^2}{2} + m^2 + k^2 \pm \Delta_t \sqrt{\frac{\Delta_t^2}{4} + m^2}}, \quad \text{(S17)}$$

where $k = \sqrt{k_x^2 + k_y^2}$. From the eigen-functions $|u_{nk}\rangle$, which corresponds to the eigen-energies E_n, we compute the Berry connection and curvature defined as $a_n(\boldsymbol{k}) = i\langle u_{nk}|\nabla_k|u_{nk}\rangle$ and $b_n(\boldsymbol{k}) = \nabla_k \times a_n(\boldsymbol{k})$, respectively. Then, the Berry curvature contribution of the Hall conductivity σ_{xy} arising from the above 4 bands is given by,

$$\sigma_{xy} = \frac{1}{2\pi} \sum_{n=1}^{4} \iint_{-\infty}^{\infty} d^2\boldsymbol{k}\, f_n(\boldsymbol{k}) b_n(\boldsymbol{k}), \quad \text{(S18)}$$

where $f_n(\boldsymbol{k}) \equiv 1/(e^{(E_n - E_F)/k_B T} + 1) \rightarrow \theta(E_F - E_n)$ (when $T \rightarrow 0$) is the Fermi distribution function and θ is the Heaviside step function[32].

In Fig. S11A, we show the low-energy bands at the zero-temperature limit, where the hybridization is not included ($m = 0$). The red lines indicate the top surface state which has the magnetic gap ($\Delta_t = 2$), whereas the blue lines indicate the bottom surface state which has no gap ($\Delta_b = 0$). Then, the calculated σ_{xy} is shown in Fig. S11B, exhibiting a plateau structure with the half-integer quantized value when E_F locates within the magnetic gap.

We then include the hybridization term ($m \neq 0$). Figure S11C shows the numerically calculated bands including finite m ($= \Delta_t / 2 = 1$) that exhibits a gap near $E = 0$. This gap is a trivial one because σ_{xy} becomes zero when E_F is within the gap as shown in Fig. S11D, indicating that the system no longer exhibits the half-integer quantization in the presence of hybridization. We note that, when E_F intersects the bands, σ_{xy} has a non-zero value (but lower than the half-quantized value). Also, there are peaks at the band edges of the highest and lowest bands. These features are indeed observed experimentally as follows.

Experiment

We have examined 7-nm-thick films (Fig. S12A), which possess sizeable hybridization gaps comparable to their magnetization gaps[8]. We note that besides our previous study[8], the effect of the hybridization in Cr-doped (Bi, Sb)$_2$Te$_3$ films has been reported by other groups using different film thickness: 5 QL (ref. 33) and 6 QL (ref. 34), while it has also been reported in the angle-resolved photoemission study of < 2 QL Bi$_2$Te$_3$ (ref. 35) and the scanning tunneling spectroscopy study of < 4 QL Sb$_2$Te$_3$ (ref. 36). This controversy on the critical film thickness may arise from the difference between experimental techniques, namely transport, photoemission, and local tunneling spectroscopy; the detailed calibration of the critical thickness is still under debate.

Figure S12B shows the V_g dependence of σ_{xy} in the film of $x = y = 0.88$ which we have presented in our previous publication[23], where E_F is supposed to be above the magnetic gap of the top surface state and is slightly below the Dirac point for the bottom surface state as judged from the results presented in Fig. S6. In contrast to the half-integer quantization in 10-nm-thick films presented in the main text, the half-quantized σ_{xy} does not appear at $\mu_0 H = 0$ T while the $\nu = 0$ and 1 QH plateaus emerge at $\mu_0 H = 14$ T.

Furthermore, we observe a dip at around $V_g = 0$ V. Within this dip, σ_{xx} also takes a minimum value (Fig. S12C). This indicates the hybridization-induced trivial gap as expected from the numerical results shown in Fig. S12D. We have additionally checked another sample in which we finely tuned E_F within the magnetic gap of the top surface ($x = 0.73$, $y = 0.85$), leading to an even more insulating state (Figs. S12D and S12E). We then map ($\sigma_{xy}(T)$, $\sigma_{xy}(T)$) at the most insulating V_g (Fig. S12F) for the two samples, flowing to the trivial insulating fixed point (0, 0). In conclusion, thickening the films to suppress the surface hybridization is required to observe the half quantized σ_{xy}.
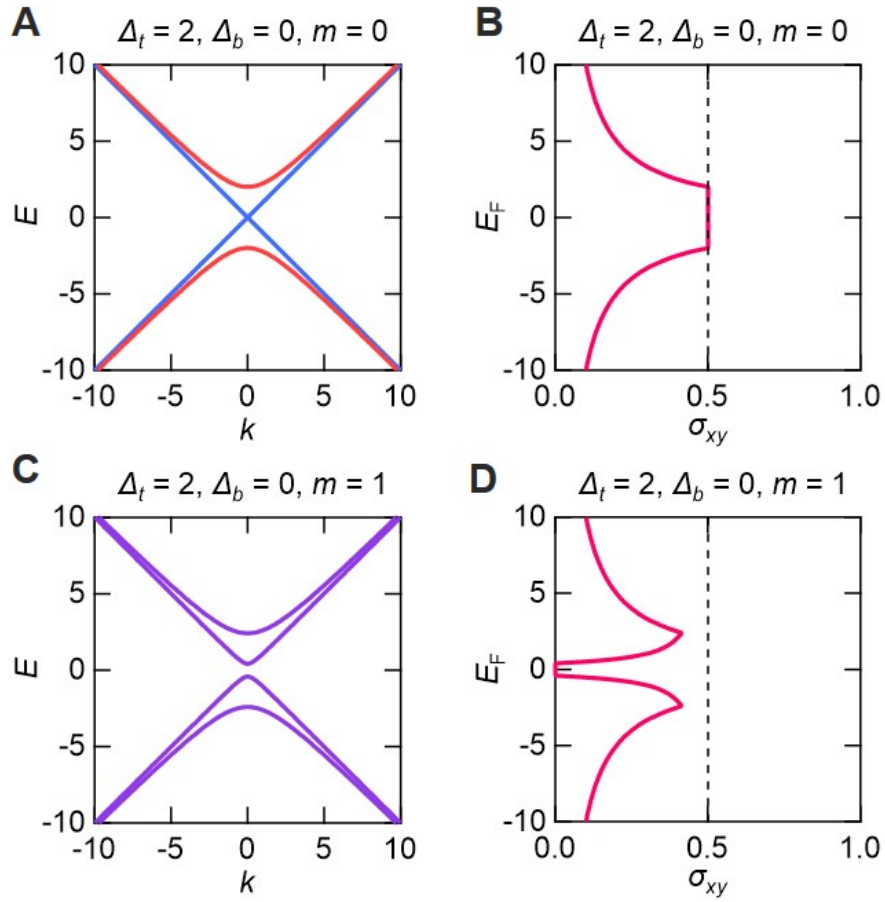
Fig. S11. Calculated Hall conductivity including surface hybridization. (**A**, **C**) Low-energy bands calculated for the continuum model including $\Delta_t = 2$, $m = 0$ (A) and $\Delta_t = 2$, $m = 1$ (C). (**B**, **D**) Calculated σ_{xy} versus E_F corresponding to the band structures in (A) and (C), respectively.
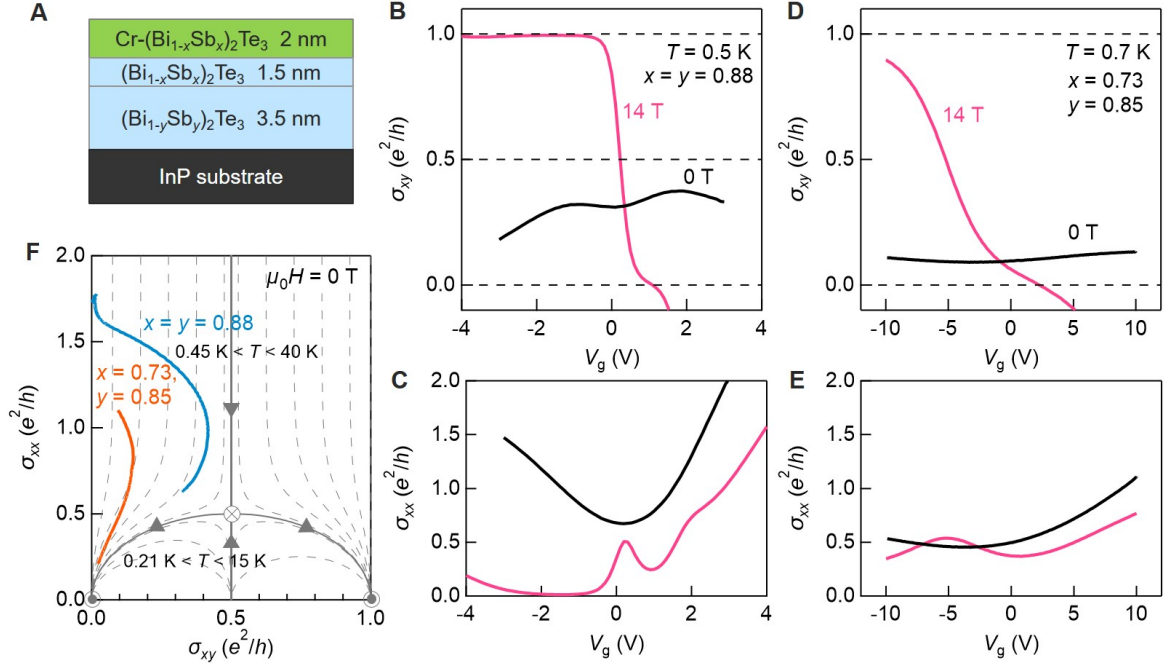
Fig. S12. Surface-hybridization-induced trivial insulator phase in thin semi-magnetic TI films. (**A**) Schematic layout of the 7-nm-thick semi-magnetic TI films studied in (B-F). (**B, C**) V_g dependence of σ_{xy} and σ_{xx} in a semi-magnetic TI film ($x = y = 0.88$) at $T = 0.5$ K and $\mu_0H = 0$, 14 T, reproduced from ref. 27. (**D, E**) V_g dependence of σ_{xy} and σ_{xx} in a semi-magnetic TI film ($x = 0.73$, $y = 0.85$) at $T = 0.7$ K and $\mu_0H = 0$, 9 T. (**F**) T-driven flows of (σ_{xy}, σ_{xx}) at $\mu_0H = 0$ T.

XI. Dependence of the sample size on transport.

We fabricated multiple Hall bars with various widths $W = 10$ μm to 1.5 mm, where the distance between the voltage probes is fixed at $L = W$ and that between the source and drain is kept to $> 3L$. Figure S13C shows the robustness of the half quantized σ_{xy} obtained from resistance data shown in Fig. S13A,B. We observe that σ_{xx} increases with thinning the Hall bars (Fig. S13D). We speculate that the change of σ_{xx} comes from a finite localization length which might be larger than the present sample size W.
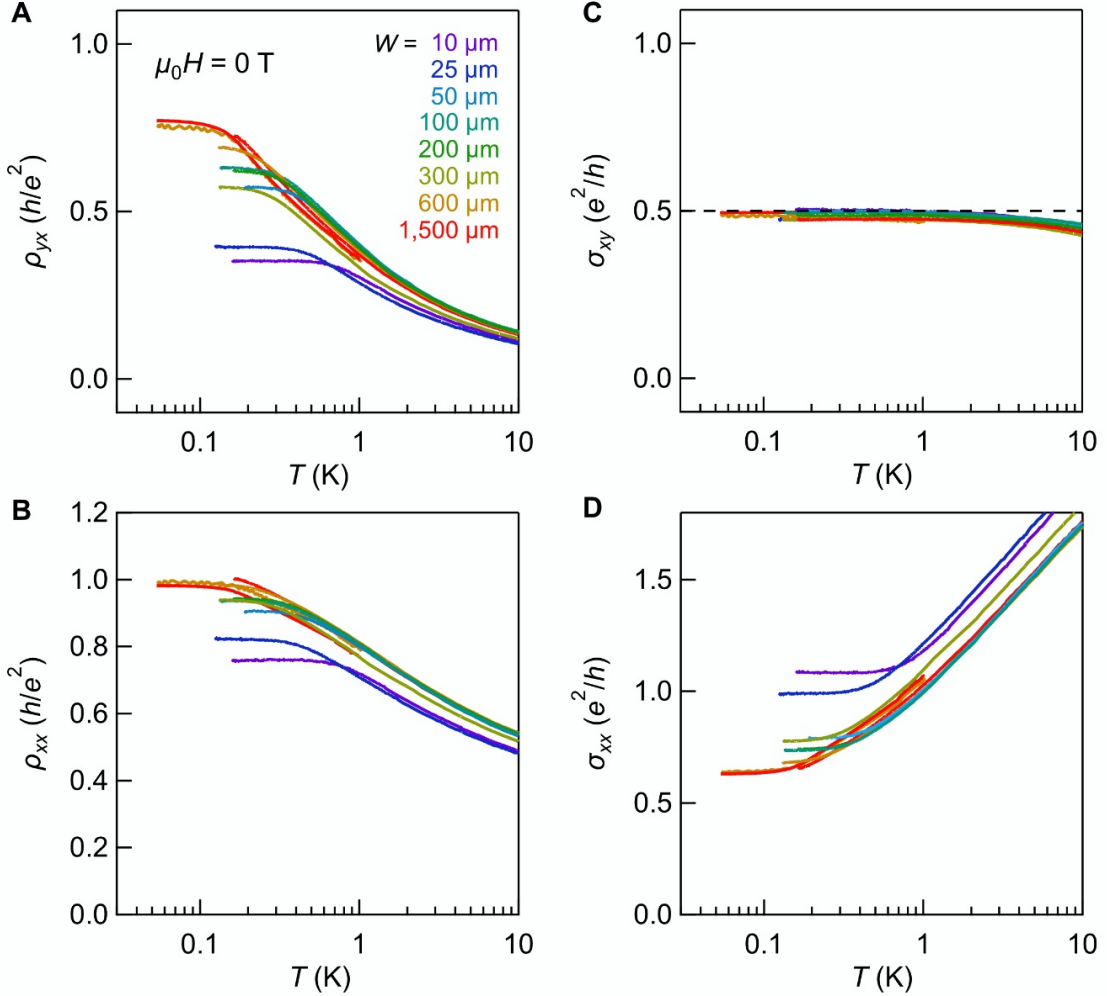
Fig. S13. Sample width dependence. (A-D) ρ_{yx} (A), ρ_{xx} (B), σ_{xy} (C), σ_{xx} (D) as a function of T in a logarithmic scale at $\mu_0 H = 0$ T in semi-magnetic TI films ($x = 0.85$) with various sample width W.

XII. Half-integer quantized transport in a V-doped semi-magnetic TI

We tried a similar transport experiment on another QAH system[37,38] – 3-nm V-doped $(Bi,Sb)_2Te_3$ / 6-nm $(Bi,Sb)_2Te_3$ semi-magnetic structure (Fig. S14A). As shown in Fig. S14B, C, we indeed obtained a similar half-integer Hall conductivity at zero magnetic field. This suggests that the half-integer quantization is robust against the changes of thickness and doping element/concentration.
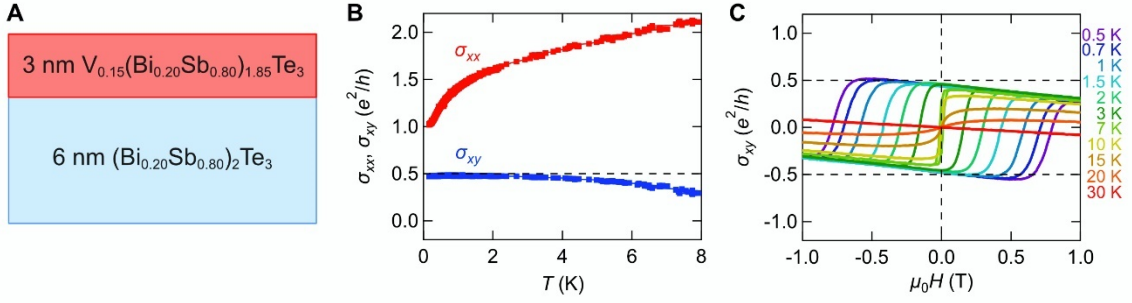
Fig. S14. Transport measurement of a V-doped semi-magnetic TI. (A) Schematic layout of a V-doped semi-magnetic TI film. **(B)** Temperature dependence of σ_{xx} and σ_{xy} at zero magnetic field once after training the magnetization up to 3 T at the lowest temperature. **(C)** Magnetic field dependence of σ_{xy} at various temperatures. Note that the field-induced change of σ_{xy} comes from an ordinary Hall effect while the spontaneous component of σ_{xy} at zero magnetic field corresponds to the anomalous Hall effect.

Supplementary References

1. Niemi, A. J. & Semenoff, G. W. Axial-anomaly-induced fermion fractionization and effective gauge-theory actions in odd-dimensional space-times. *Phys. Rev. Lett.* **51**, 2077-2080 (1983).

2. Redlich, A. N. Gauge noninvariance and parity nonconservation of three-dimensional fermions. *Phys. Rev. Lett.* **52**, 18-21 (1984).

3. Jackiw, R. Fractional charge and zero modes for planer systems in a magnetic field. Phys. Rev. D **29**, 2375-2377 (1984).

4. Semenoff, G. Condensed-matter simulation of a three-dimensional anomaly. *Phys. Rev. Lett.* **53**, 2449-2452 (1984).

5. Fradkin, E., Dagotto, E. & Boyanovsky, D. Physical realization of the parity anomaly in condensed matter physics. *Phys. Rev. Lett.* **57**, 2967-2970 (1986).

6. Haldane, F. D. M. Model for a quantum Hall effect without Landau levels: Condensed-matter realization of the "parity anomaly". *Phys. Rev. Lett.* **61**, 2015-2018 (1988).

7. Nielsen, N. B. & Ninomiya, M. Absence of neutrinos on a lattice: (I). Proof by homotopy theory. *Nucl. Phys.* **B185**, 20-40 (1981).

8. Kawamura, M. et al. Topological quantum phase transition in magnetic topological insulator upon magnetization rotation. *Phys. Rev. B* **98**, 140404(R) (2018).

9. Mogi, M. et al. Magnetic modulation doping in topological insulators toward higher-temperature quantum anomalous Hall effect. *Appl. Phys. Lett.* **107**, 182401 (2015).

10. Mogi, M. et al. A magnetic heterostructure of topological insulators as a candidate for an axion insulator. *Nat. Mater.* **16**, 516-521 (2017).

11. Zhao, Y.-F. et al. Tuning the Chern number in quantum anomalous Hall insulators. *Nature* **588**, 419-423 (2020).

12. Zhang, J. et al. Topology-driven magnetic quantum phase transition in topological insulators. *Science* **339**, 1582-1586 (2013).

13. Szénchenyi, G., Vigh, M., Kormányos, A. & Cserti, J. Transfer matrix approach for the Kerr and Faraday rotation in layered nanostructures. *J. Phys.: Condens. Matter* **28**, 375802 (2016).

14. Lee, I. et al. Imaging Dirac-mass disorder from magnetic dopant atoms in the ferromagnetic topological insulator $Cr_x(Bi_{0.1}Sb_{0.9})_{2-x}Te_3$. *Proc. Natl. Acad. Sci. USA* **112**, 1316-1321 (2015).

15. Jiang, Y. et al. Mass acquisition of Dirac fermions in magnetically doped topological insulator Sb_2Te_3 films. *Phys. Rev. B* **92**, 195418 (2015).

16. Lachman, E. O. et al. Visualization of superparamagnetic dynamics in magnetic topological insulators. *Sci. Adv.* **10**, e1500740 (2015).

17. Yasuda, K. et al. Quantized chiral edge conduction on domain walls of a magnetic topological insulator. *Science* **358**, 1311-1314 (2017).

18. Wang, W. et al. Direct evidence of ferromagnetism in a quantum anomalous Hall system. *Nat. Phys.* **14**, 791-795 (2018).

19. Bestwick, A. J. et al. Precise quantization of the anomalous Hall effect near zero magnetic field. *Phys. Rev. Lett.* **114**, 187201 (2015).

20. Iguchi, S. et al. Optical probe for anomalous Hall resonance in ferromagnets with spin chirality. *Phys. Rev. Lett.* **103**, 267206 (2009).

21. Tse, W.-K. & MacDonald, A. H. Giant magneto-optical Kerr effect and universal Faraday effect in thin-film topological insulators. *Phys. Rev. Lett.* **105**, 057401 (2010).

22. Chapler, B. C. et al. Infrared electrodynamics and ferromagnetism in the topological semiconductors Bi_2Te_3 and Mn-doped Bi_2Te_3. *Phys. Rev. B* **89**, 235308 (2014).

23. Yoshimi, R. et al. Quantum Hall states stabilized in semi-magnetic bilayers of topological insulators. *Nat. Commun.* **6**, 8530 (2015).

24. Huckestein, B. Scaling theory of the integer quantum Hall effect. *Rev. Mod. Phys.* **67**, 357 (1995).

25. Akiho, T., Irie, H., Onomitsu, K. & Muraki, K. Counterflowing edge current and its equilibration in quantum Hall devices with sharp edge potential: Roles of incompressible strips and contact configuration. *Phys. Rev. B* **99**, 121303(R) (2019).

26. Pruisken, A. M. M. Universal singularities in the integral quantum Hall effect. *Phys. Rev. Lett.* **61**, 1297 (1988).

27. Dolan, B. P. Modular invariance, universality, and crossover in the quantum Hall effect. *Nucl. Phys. B* **554**, 487-513 (1999).

28. Nomura, K. & Nagaosa, N. Surface-quantized anomalous Hall current and the magnetoelectric effect in magnetically disordered topological insulators. *Phys. Rev. Lett.* **106**, 166802 (2011).

29. Checkelsky, J. G. et al. Trajectory of the anomalous Hall effect towards the quantized state in a ferromagnetic topological insulator. *Nat. Phys.* **10**, 731-736 (2014)

30. Nomura, K., Koshino, M. & Ryu, S. Topological delocalization of two-dimensional massless Dirac fermions. *Phys. Rev. Lett.* **99**, 146806 (2007).

31. Wang, J., Lian, B. & Zhang, S.-C. Quantum anomalous Hall effect in magnetic topological insulators. *Phys. Scr.* **T164**, 014003 (2015).

32. Nagaosa, N., Sinova, J., Onoda, S., MacDonald, A. H. & Ong, N. P. Anomalous Hall effect. *Rev. Mod. Phys.* **82**, 1539 (2010).

33. Feng, Y. et al. Observation of the zero Hall plateau in a quantum anomalous Hall insulator. *Phys. Rev. Lett.* **115**, 126801 (2015).

34. Kou, X. et al. Metal-to-insulator switching in quantum anomalous Hall states. *Nat. Commun.* **6**, 8474 (2015).

35. Li, Y.-Y. et al. Intrinsic topological insulator Bi_2Te_3 thin films on Si and their thickness limit. *Adv. Mater.* **22**, 4002-4007 (2010).

36. Jiang, Y. et al. Landau quantization and the thickness limit of topological insulator thin films of Sb_2Te_3. *Phys. Rev. Lett.* **108**, 016401 (2012).

37. Chang, C.-Z. et al. High-precision realization of robust quantum anomalous Hall state in a hard ferromagnetic topological insulator. *Nat. Mater.* **14**, 473-477 (2015).

38. Mogi, M. et al. Tailoring tricolor structure of magnetic topological insulator for robust axion insulator. *Sci. Adv.* **3**, eaao1669 (2017).